EARTH SURFACE PROCESSES AND LANDFORMS
Earth Surf. Process. Landforms (2015)

Published online in Wiley Online Library
(wileyonlinelibrary.com) DOI: 10.1002/esp.3787

Assessing the performance of structure-from-motion photogrammetry and terrestrial LiDAR for reconstructing soil surface microtopography of naturally vegetated plots

Sayjro Kossi Nouwakpo,[1]* Mark A. Weltz[2] and Kenneth McGwire[3]
[1] Natural Resources and Environment Sciences, University of Nevada Reno, Reno, NV, USA
[2] USDA-ARS Exotic and Invasive Weeds Research Unit, Reno, NV, USA
[3] Desert Research Institute Earth and Ecosystem Sciences, Reno, NV, USA

Received 6 October 2014; Revised 23 June 2015; Accepted 6 July 2015

*Correspondence to: Sayjro Kossi Nouwakpo, Natural Resources and Environment Sciences, University of Nevada Reno, 1664 North Virginia Street, Reno, NV 89557, USA. E-mail: snouwakpo@unr.edu

ESPL
Earth Surface Processes and Landforms

ABSTRACT: Soil microtopography is a property of critical importance in many earth surface processes but is often difficult to quantify. Advances in computer vision technologies have made image-based three-dimensional (3D) reconstruction or Structure-from-Motion (SfM) available to many scientists as a low cost alternative to laser-based systems such as terrestrial laser scanning (TLS). While the performance of SfM at acquiring soil surface microtopography has been extensively compared to that of TLS on bare surfaces, little is known about the impact of vegetation on reconstruction performance. This article evaluates the performance of SfM and TLS technologies at reconstructing soil microtopography on 6 m × 2 m erosion plots with vegetation cover ranging from 0% to 77%. Results show that soil surface occlusion by vegetation was more pronounced with TLS compared to SfM, a consequence of the single viewpoint laser scanning strategy adopted in this study. On the bare soil surface, elevation values estimated with SfM were within 5 mm of those from TLS although long distance deformations were observed with the former technology. As vegetation cover increased, agreement between SfM and TLS slightly degraded but was significantly affected beyond 53% of ground cover. Detailed semivariogram analysis on meter-square-scale surface patches showed that TLS and SfM surfaces were very similar even on highly vegetated plots but with fine scale details and the dynamic elevation range smoothed out with SfM. Errors in the TLS data were mainly caused by the distance measurement function of the instrument especially at the fringe of occlusion regions where the laser beam intersected foreground and background features simultaneously. From this study, we conclude that a realistic approach to digitizing soil surface microtopography in field conditions can be implemented by combining strengths of the image-based method (simplicity and effectiveness at reconstructing soil surface under sparse vegetation) with the high accuracy of TLS-like technologies.

KEYWORDS: photogrammetry; Structure-from-Motion; SfM; LiDAR; TLS; soil microtopography; DEM; soil erosion

Introduction

Understanding sediment redistribution along transient landscape positions is essential to addressing most erosion, sedimentation and contaminant loading problems. At the hillslope scale, various techniques have been developed to quantify erosion and deposition processes. Toy *et al.* (2002) distinguish four fundamental ways to measure erosion including: (1) change in weight often limited to laboratory or field experiments on small soil samples; (2) change in surface elevation; (3) change in channel cross-section dimensions; (4) sediment collection from erosion plots and watersheds. While sediment collection techniques are simple and reliable, they are inadequate to quantify deposition processes and lead to loss of spatial resolution because transport processes are spatially lumped into runoff samples. Techniques based on soil surface elevation (or microtopography) changes may not directly relate to masses of soil moved in some cases due to the grain size selectivity of erosion and deposition processes and to the microscopic contribution of the soil colloidal fraction to soil surface elevation (Heng *et al.*, 2010; Nouwakpo and Huang, 2012b). Nevertheless, changes in soil microtopography provide valuable information on spatial redistribution of sediments following erosive events (e.g. Rieke-Zapp and Nearing, 2005; Berger *et al.*, 2010; Heng *et al.*, 2011; Nouwakpo and Huang, 2012b). In addition, soil microtopography is useful in describing other physical, hydrologic and biological processes. It was shown for example to control infiltration and runoff amounts (Romkens *et al.*, 2001; Thompson *et al.*, 2010) and plays a central role in ecohydrologic processes such as rainwater redistribution, seed displacement and plant competition (Rossi and Ares, 2012b).

Existing soil microtopography survey methods

Early soil microtopography acquisition devices estimate surface elevation from mechanical relief meters consisting of regularly spaced needles that are mobile in the vertical direction along a one-dimensional horizontal frame. Mechanical relief meters have been used in many soil erosion studies to characterize soil surface microtopography (e.g. Guzha, 2004; Moreno *et al.*, 2008) or track changes resulting from erosion (Kincaid and Williams, 1966; Elliot *et al.*, 1997). Because the contact required between these mechanical devices and the soil surface is associated with measurement biases and surface disturbances, non-contact elevation measurement devices are preferred (Jester and Klik, 2005). Laser scanners and image-based three-dimensional (3D) reconstruction have been the most commonly used technologies for non-contact soil microtography measurement.

Laser-based technologies use a triangulation system consisting of a laser light source and either an image acquisition device measuring the angle of the laser light reflected from the soil surface (Helming *et al.*, 1998; Romkens *et al.*, 2001; Darboux and Huang, 2003) or a time of travel measurement system measuring the distance between to the soil surface at a known instrument orientation. The latter laser-based technology also known as light detection and ranging (LiDAR) has been used for high resolution soil microtopography measurement in the fields of hydrology and ecohydrology (e.g. Roering *et al.*, 2009; Eitel *et al.*, 2011; Castillo *et al.*, 2012; Sankey *et al.*, 2012). Laser technologies are often assumed to be highly accurate and generate scaled elevation models but their traditionally high hardware acquisition cost and bulk limits their widespread use.

Image-based 3D reconstruction technologies can be categorized in two broad groups: traditional stereo-photogrammetry and Structure-from-Motion (SfM) photogrammetry. The fundamental difference between SfM and traditional photogrammetry lies in the steps required for 3D scene reconstruction. Traditional photogrammetry requires a priori knowledge of the camera position and orientation before reconstructing a 3D scene. This camera pose information is typically solved from ground control points (GCPs) that often need to be manually identified in the images by the user. In the very specific cases of imaging systems equipped with global positioning and inertial measurement units, camera pose can also be initialized from position and orientation metadata. Traditional stereo-photogrammetry was used in early attempts to apply image-based 3D reconstruction to acquire soil surface microtopography (e.g. Lo and Wong, 1973; Collins and Moon, 1979; Valentine and Cook, 1979). Over the years, traditional photogrammetry which was historically considered an impractical technology due to its reliance on expensive hardware, software and trained personnel has benefited from various technological advances (e.g. advent of digital cameras, progress in lens manufacturing and semi-automation of key photogrammetric steps) leading to its increased use for soil microtopography acquisition in both close-range (e.g. Barker *et al.*, 1997; Aguilar *et al.*, 2009; Berger *et al.*, 2010; Heng *et al.*, 2010; Nouwakpo and Huang, 2012a) and low-altitude aerial applications (e.g. Ries and Marzolff, 2003; Marzolff and Poesen, 2009).

During the past two decades, advances in computer vision led to the development of SfM technology which significantly simplified image-based surface reconstruction. In contrast to stereo-photogrammetry, SfM solves 3D scene structure and camera pose simultaneously by making use of advanced image feature detection and matching techniques (e.g. Harris and Stephens, 1988; Lowe, 1999; Bay *et al.*, 2006) and a highly redundant bundle adjustment procedure, allowing for a simplified workflow for 3D reconstruction. With this new approach, a 3D point cloud in an arbitrary model coordinate system is created and can be appropriately scaled and oriented by applying a simple 3D similarity transformation to targets of which only ground and model space 3D coordinates need to be known (Westoby *et al.*, 2012). Although the SfM approach often leads to lower accuracy compared to the more rigorous traditional photogrammetry (James and Robson, 2012), it offers the advantage of simpler implementation. In addition, the interest of geoscientists in this technology as a surface reconstruction tool has been heightened by the development of freely available SfM software (e.g. Castillo *et al.*, 2012; James and Robson, 2012; Westoby *et al.*, 2012) and the emergence of low cost unmanned aerial vehicles used as convenient platforms for large-scale projects (e.g. Rosnell and Honkavaara, 2012; Mancini *et al.*, 2013; Javemick *et al.*, 2014; Ouedraogo *et al.*, 2014).

Aims of this study

The performance of SfM as earth surface reconstruction technology has been evaluated against various alternative technologies such as traditional photogrammetry (e.g. James and Robson, 2014b; Nouwakpo *et al.*, 2014), total station and laser profilemeter (Castillo *et al.*, 2012), aerial (e.g. Johnson *et al.*, 2014) and terrestrial (e.g. Castillo *et al.*, 2012; Mancini *et al.*, 2013; Gomez-Gutierrez *et al.*, 2014; James and Quinton, 2014; Johnson *et al.*, 2014; Kaiser *et al.*, 2014) LiDAR as well as real-time kinematic systems (Mancini *et al.*, 2013). In the aforementioned studies comparing SfM to terrestrial LiDAR (or terrestrial laser scanning [TLS]) systems the latter technology has often been used as benchmark because of the well-documented performance of this tool in geosciences (Castillo *et al.*, 2012).

TLS and SfM technologies often show appreciable discrepancies in the presence of vegetation on the surveyed areas (e.g. Castillo *et al.*, 2012; Mancini *et al.*, 2013). Vegetated patches often cause abrupt near-vertical changes in surface elevation, occlude soil surface and are susceptible to detrimental wind-driven motion, thus challenging both SfM and TLS technologies. Many geoscience processes associated with soil surface microtopography occur on naturally vegetated surfaces. Nevertheless, few guidelines exist for the acquisition and treatment of SfM data on vegetated surfaces. Also, the range and characteristics of vegetative cover under which useful soil microtopography information can be recovered is unclear. The aim of this article is to evaluate the performance of SfM in comparison to TLS at reconstructing soil microtopography on a range of natural vegetation covers and characteristics in order to provide application recommendations for vegetated surfaces.

Material and Methods

Hardware used

A Canon EOS Digital Rebel XT camera with a nominal fixed focal length of 20 mm was used to acquire images used in SfM reconstructions. The camera lens was set to manual focus after adjusting it to the average camera – soil surface distance of 2 m for this project. The lens was then taped to avoid accidental changes to focus setting and internal camera calibration.

In this study, GCPs were used on each plot to register and orient SfM reconstructions. A basic spatial arrangement of 10 GCPs per plot was sought: four evenly distributed along each long side and one centered at 0.20 m from upslope and downslope boundaries (Figure 1). Because of the occluding effect of vegetation (especially that of shrubs), up to 15 GCPs were used per plot however, to ensure that enough GCPs were common to both SfM and TLS datasets. Additional GCPs were mainly placed along the long sides of each plot at positions that appeared to be visible by both technologies. GCPs were 5 cm plastic squares printed with a checkerboard pattern and mounted on 15 cm anchoring pins. A Nikon NPR 352 total station was used to measure GCP coordinates in reflectorless mode to avoid physical contact with the soil surface. Average vertical and positional precisions achieved with the NPR 352 in this study were respectively 0.4 and 3 mm.

A Leica ScanStation 2 was used to provide an independent source of precise 3D coordinates for the soil surface and vegetation in each plot. The ScanStation 2 is controlled by a laptop computer and collects co-registered color photographs along with the 3D point cloud. Scans of each plot were conducted with a 2.0 mm spacing at mid-plot. The hemispherical sampling pattern resulted in finer density at the plot outflow end (approximately 0.5 mm) and coarser density at the upslope end (approximately 8 mm). The standard deviation of sampling distances across the entire plot was 1.7 mm.

Erosion plot

Soil microtopography data used in this study were collected during a series of rainfall simulation experiments aiming at testing a suite of technologies specifically developed for plot scale erosion studies in rangeland environment. A Walnut Gulch Rainfall Simulator (WGRS) (Paige *et al.*, 2004) was used for this study (Figure 2). The WGRS has an effective spray area of 6.1 m × 2 m which determined the 6 m × 2 m size of erosion plots used in this study.

Erosion plots were selected to test SfM and TLS technologies on a range of vegetation canopy covers and ground covers. Tests on bare ground were performed on a 6 m × 2 m outdoor-laboratory rainfall simulation plot while vegetated plots were selected on a reclaimed construction site. Six vegetated plots were selected corresponding to ground occlusion (GO) by live vegetation and litter of 14%, 23%, 53%, 64% and 77% and identified as GO14, GO23, GO53, GO64 and GO77, respectively (Figure 3). The bare laboratory erosion plot is identified here as GO0. Detailed plot cover characteristics are summarized in Table I.

Data processing and software used

Images used for SfM reconstruction were taken with the camera either mounted on a pole or handheld. The rainfall simulation experiments in this study were carried out over the course of three consecutive years. The first two years, image acquisition for surface reconstruction was initially planned to accommodate the traditional photogrammetry software Leica Photogrammetry Suite (LPS) (Leica Geosystems, 2006). Since LPS was designed to process near-vertical aerial photography, the camera was mounted the first two years on a pole with a near-nadir orientation of the imaging plane with respect to the soil surface (Figure 4a). After successfully experimenting with the SfM technology, a more oblique image network was adopted the third year with the camera handheld (Figure 4b). The handheld configuration, allowed a highly oblique and convergent camera orientation which was expected to improve reconstruction performance (Mikhail *et al.*, 2001; James and Robson, 2014a) and also reduced soil surface occlusion by vegetation. A summary of the image acquisition field protocol and resulting SfM parameters are presented in Table I.

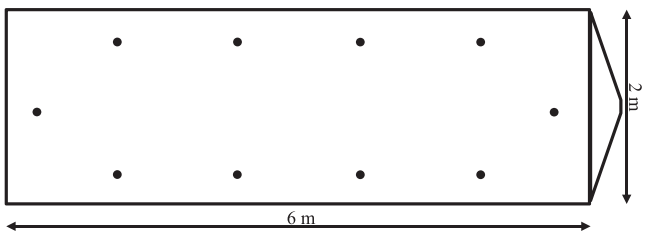

Figure 1. Schematic of the spatial distribution of GCPs (black dots) sought on each erosion plot.

In this study, SfM reconstructions were performed using the commercial software PhotoScan (Agisoft LLC, 2013). The following approach was used by PhotoScan to generate 3D surfaces:

1. Overlapping soil surface images were imported into PhotoScan.
2. PhotoScan detected salient soil surface features and matched these features between images. To detect and describe image features, PhotoScan uses an undisclosed algorithm similar to SIFT (Lowe, 1999). In our study, the effective overlap achieved by PhotoScan (number of views in which scene features were successfully matched) was on average 4.18, with a high value of 5.66 for the GO23 plot (Table I). The effective overlap is a function of various factors including image spatial overlap (actual scene common to multiple images), performance of image feature descriptor and accuracy of 3D reconstruction.
3. A sparse 3D reconstruction was performed by PhotoScan using feature points image coordinates as observations and solving simultaneously for camera exterior orientation (position and rotation) and intrinsic calibration parameters. This step along with step (2) are the core of the SfM methodology in PhotoScan.
4. The sparse 3D reconstruction was then refined and referenced to a metric coordinate system by providing to PhotoScan image and ground coordinates of surveyed GCPs. A non-linear optimization strategy in which both camera pose and interior orientation parameters were adjusted to minimize error at GCP coordinates. The average root mean square error (RMSE) achieved at this step was 0.0025 m for ground coordinates and 0.3 pixels for image coordinates. The GCP RMSE encompasses both errors in the GCP survey with the total station and intrinsic precision of the sparse SfM reconstruction. The precision of SfM at predicting 3D point position was estimated as the RMSE of modeled GCP coordinates from the series of reconstructions obtained before and after rainfall events on each plot. Since GCPs were non-erodible, variability in the GCP coordinates indicate the level of precision achieved after repeated soil surface measurements. The average positional and vertical precisions achieved in this study were respectively 0.3 mm and 0.2 mm.
5. Finally, a Multi-view Stereo (MVS) algorithm (also undisclosed) was implemented by PhotoScan to produce a dense 3D point cloud from the refined intrinsic calibration and ground-referenced camera exterior orientation.

Table II summarizes quality settings used in PhotoScan for the sparse and dense 3D reconstructions. For the dense 3D

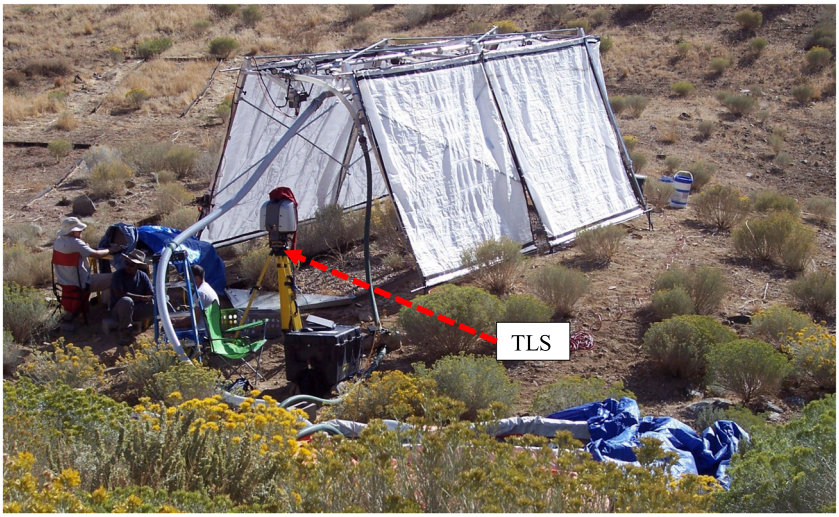

Figure 2. Picture of the rainfall simulation setup showing the terrestrial laser scanner at its scanning station. This figure is available in colour online at wileyonlinelibrary.com/journal/espl

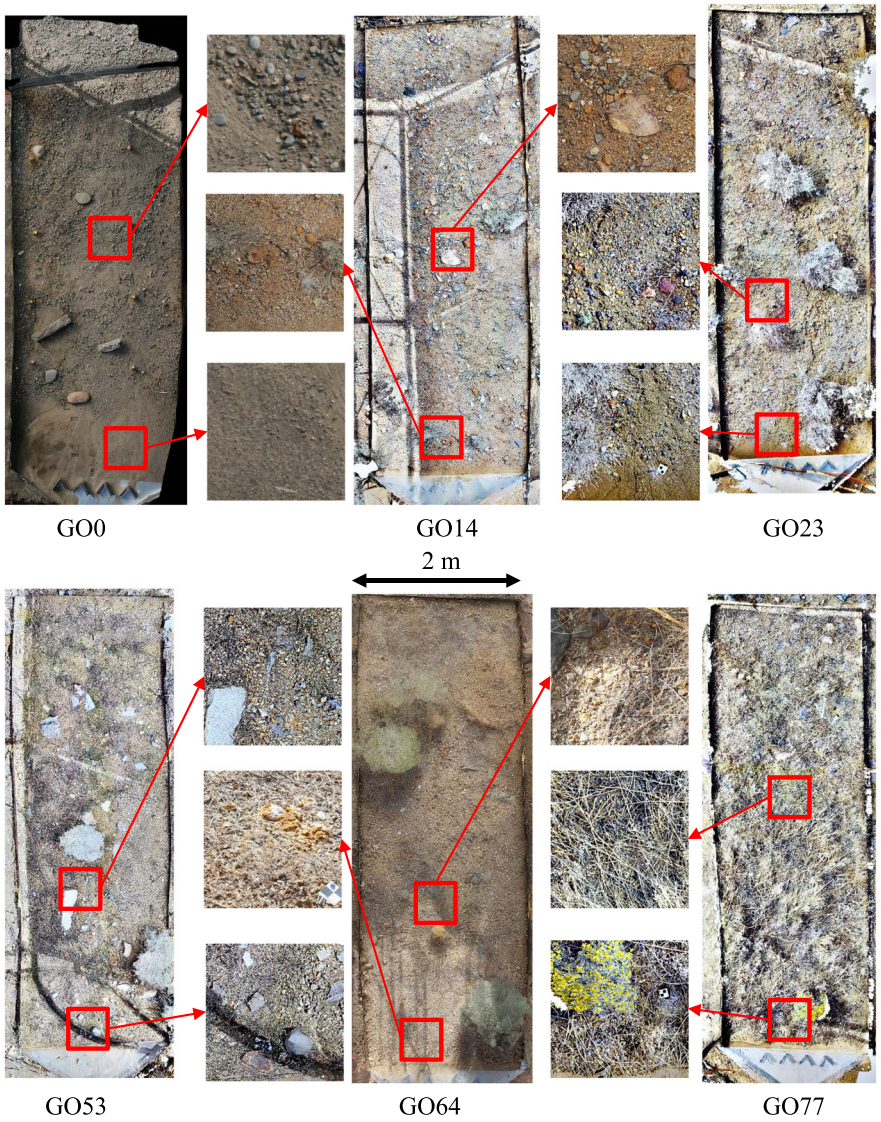

Figure 3. Synoptic and close-up views of plots GO0, GO14, GO23, GO53, GO64, and GO77. Each close-up view window is approximately 0.6 m × 0.6 m. This figure is available in colour online at wileyonlinelibrary.com/journal/espl

reconstruction PhotoScan also provides an 'Ultra High' quality setting in which depth estimation is performed on the original images but this option resulted in excessively long computation time (>24 hours) in our study. Also, the more aggressive depth filtering strategy was preferred because a high degree of 3D reconstruction noise was anticipated from vegetation.

Table I. Summary of plot surface conditions and image capture information

Plot ID	% Ground occlusion	% Canopy cover	% Litter cover	Camera support	Number of pictures	Effective overlap[a]
GO0	—	—	—	Pole	25	5.39
GO14	14.10	3.60	11.80	Handheld	127	3.50
GO23	23.18	15.90	15.00	Pole	72	5.66
GO53	53.90	23.70	45.21	Handheld	143	3.09
GO64	64.50	10.90	61.36	Handheld	282	3.83
GO77	77.72	27.27	74.09	Pole	145	3.55

[a]Average number of pictures in which each scene feature was successfully detected.

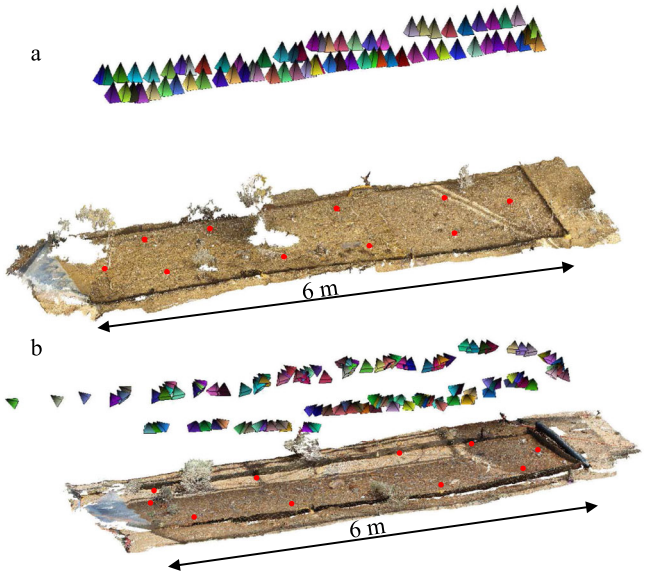

Figure 4. Perspective view of three-dimensional reconstructions showing image network for (a) the camera-on-pole and (b) ground-based camera configurations. Red dots mark ground control point locations. This figure is available in colour online at wileyonlinelibrary.com/journal/espl

Since this study was performed in conjunction with the operation of the WGRS, the TLS scans could only be performed from a single vantage point because the WGRS was equipped with wind screens which blocked access to the surveyed plot from three sides. This single viewpoint potentially resulted in significant amounts of the soil surface being occluded by vegetation. Therefore, results represent what was practically possible and not what might be accomplished in situations where multiple viewpoints could be acquired.

This study focuses on measurement of the soil surface, so a Java program was written to remove vegetated points from the SfM and TLS products. A number of freely available software for LiDAR analysis were tested, but those programs were developed for airborne LiDAR and had significant problems with the irregular sample spacing of the hemispherical TLS scans and occluded areas. Other examples of efforts to discriminate ground surfaces in TLS datasets include Brodu and Lague (2012), Brasington *et al.* (2012), and Rychkov *et al.* (2012). Our program estimated the soil surface using the following steps:

1. Provide a coarse estimation of soil surface by superimposing a grid and finding the lowest point within each grid cell.
2. Fit a second-order polynomial trend surface to these local minima.
3. Difference measurements from trend surface to separate local height from overall slope elevation.
4. User specifies a maximum height (0.2 m) to quickly eliminate a large number of upper vegetation points.
5. For remaining points, calculate a second-order trend surface within each grid cell and eliminate points that are greater than a user-specified number of standard deviations (1.5) above mean of remaining points (slower).
6. For remaining points, calculate the slope to neighbors within a search radius of one half the grid dimension (slowest). Find the maximum slope within each of four directional quadrants. Remove points whose minimum value of maximum slope across all quadrants is greater than a user-specified value (20°).

The strategy of using the minimum of maximum slope in each direction identified protrusions that were not part of the local trend in surface relief. User-specified values were determined through testing by two analysts with data from multiple plots. This method effectively screened vegetation while minimizing the removal of erosional features or protruding cobbles.

Since SfM and TLS point clouds were produced in different coordinate systems, they were aligned using the freely available point cloud comparison software CloudCompare V2.5 (General Public Licence, 2014). An initial alignment using a point-picking method was performed followed by a fine registration operation based on the Iterative Closest Point (ICP) method. Registered point clouds were then used for the SfM–TLS comparisons.

Reconstruction comparisons and spatial statistics analysis

To measure the effect of GO on reconstruction, the proportion of spatial gap in each point cloud was estimated by performing image analysis on nadir views of the original (with vegetation) surfaces. In addition, overall reconstruction performance was evaluated by geometrically comparing vegetation-filtered TLS point clouds to corresponding SfM point clouds. In particular, differences between point clouds were performed to check for any plot scale surface deformation often present in SfM reconstructions of weak geometric convergence (Rosnell and Honkavaara, 2012; James and Robson, 2014a; Nouwakpo *et al.*, 2014).

Available methods for comparing point clouds include: difference of digital elevation model (DoD), cloud-to-cloud closest point distance (C2C), cloud-to-mesh distance (C2M) and the model-to-model distance approach (M3C2). Lague *et al.* (2013) presented a detailed description and comparison of these techniques which are summarized here. In the DoD approach, gridded representations of surface elevation are differenced to quantify microtopographic change (e.g. Brasington and Smart, 2003; Nouwakpo and Huang, 2012b; Schneider *et al.*, 2013). This method is fast, but can result in detrimental loss of spatial information on complex surfaces with overhanging structures and is susceptible to uncertainties due to the interpolation process from point cloud to gridded data structures. The C2C method computes for each point of a reference point

Table II. Reconstruction quality settings used in PhotoScan

	Parameter	Value	Description
Feature detection, matching and sparse scene reconstruction	Accuracy	High	Preserves the original image resolution, leading to accurate pose estimation
	Key point limit	40000	Maximum number of features to detect per image
	Tie point limit	1000	Maximum number of matches to keep per image
Dense point cloud reconstruction	Quality	High	Downscales images by a factor of four before depth estimation
	Depth filtering	Aggressive	Most stringent tolerance for outlier detection

cloud, the distance to the closest point or to a locally modeled surface (height function or least square fit of closest neighbors) in the compared point cloud. The main drawback of this technique is its sensitivity to surface roughness, the presence of outliers and dependence on spatial sampling rate. In the C2M approach, change is quantified by computing the distance from every point of the compared surface to a modeled reference surface (often in the form of a 3D mesh) while the more recent M3C2 technique (Lague *et al.*, 2013) computes cloud-to-cloud distances along surface normals, thus avoiding the complex step of mesh or digital elevation model (DEM) creation.

In our study, soil surface features were characterized by millimeter-scale elevation variations over the meter-scale planimetric dimensions of the erosion plots and little overhanging structures and vertical walls (erosional channels were mostly V-shaped). The DoD approach was therefore suitable and sufficient for comparing reconstruction of soil surface features between TLS and SfM. Nevertheless, vegetation occluded under-canopy soil surface and were filtered out of each point cloud with the algorithm described earlier before interpolation into DEMs. Also, because vegetation interfered with soil surface reconstruction and resulted in GO, patches of soil surface with continuous coverage in both SfM and TLS data were selected for detailed reconstruction evaluation. This patch analysis allowed a more refined ICP registration by limiting potential registration errors due to occlusions in the plot reconstructions.

In addition to the DoD analyses, agreement between TLS and SfM reconstructions on each patch was evaluated by comparing their elevation semivariograms. A semivariogram characterizes the autocorrelation in a random process (in this case the soil surface elevation) between sample points as distance (lag) between these points increases (Cressie and Wikle, 2011). The shape of a semivariogram is commonly described using the following parameters: (1) the range is the distance at which an initially increasing semivariance levels off, indicating the range of influence of a point, (2) the value attained at the range is the sill and (3) the nugget is the semivariance at an infinitesimal small lag between points. The advantage of using the semivariogram to compare TLS and SfM reconstructions is that this method allows evaluating the match between surfaces independently of registration errors. In other words, hypothetically identical point clouds are expected to show the same elevation semivariogram regardless of any systematic registration error that may exist between them. Rough surfaces would lead to higher semivariances and stronger nugget effects compared to smooth surfaces. A detailed presentation of spatial statistics theories and the semivariogram procedure is beyond the scope of this article and the reader is referred to references on the topic (e.g. Cressie and Wikle, 2011; Schuenemeyer and Drew, 2011) for more specific information.

In the field data, two patches of approximately 2 m^2 were selected from the vegetation-filtered data (Figure 5). One patch labelled P14 was selected from plot GO14 in a region where vegetation influence was limited to sparsely distributed grass strands or litter debris. The other patch (P23) was extracted from GO23 in a plot region where two shrubs were present in addition to grass and litter debris. These patches were selected close to the TLS viewpoint (downstream end of the plots) where TLS point density was the highest and vegetation occlusion was minimal. This choice of patch location allowed a comparison of SfM to TLS at its full potential and mitigated any comparison bias that may have been introduced by the single viewpoint scanning strategy. Due to the large amounts of data contained in each original point clouds, each patch had to be subsampled to a maximum of 20 000 points. This subsampling procedure facilitated the otherwise computer-intensive semivariogram computation step.

Data from the laboratory simulation plot was ideal to study intrinsic TLS and SfM performances with no vegetation influence. A series of rainfall simulation experiments on this laboratory plot have created a sorting of soil particles and aggregates in the downslope direction with a pebbly soil surface in the active erosion zone approximately 2 m from the downslope end of the plot and a smooth (low texture) deposition region at the downslope end of the plot. Since SfM relies on accurate matching of salient image features, surface smoothness is expected to influence reconstruction quality. The smooth and pebbly vegetation free soil surface conditions were therefore used to determine the effect of surface smoothness on SfM reconstruction by comparison to the TLS system. For this purpose, four patches were selected on plot GO0. Two of these patches were selected in the deposition area ($P0_{DL}$ and $P0_{DS}$) and two patches in the active erosion area ($P0_{EL}$, $P0_{ES}$). $P0_{DL}$ and $P0_{EL}$ are approximately 1.5 m^2 in size and are expected to describe surface conditions at a scale comparable to that of P14 and P23 and were subsampled to 20 000 points. $P0_{DS}$ and $P0_{ES}$ are approximately 0.6 m^2 in size and were left in their original point density to describe fine-scale soil surface variations.

Results

Overall reconstruction evaluation

Results of the effects of GO on TLS and SfM on soil surface reconstructions are summarized in Table III. Overall, the single viewpoint TLS data was several times more susceptible to GO than SfM. The proportion of missing point gaps was not directly correlated to percent ground cover data. For example the moderately vegetated GO23 plot resulted in an appreciably higher proportion of missing point gaps (30.7%) compared to the more densely vegetated GO77 plot (23.0%). Patterns of missing points in the TLS data were instead controlled by the geometry of shadows projected by plants relative to the oblique point of view of the TLS (Figure 5). As an example, plots with the highest proportion of missing point gaps (e.g. GO23 and GO64) also contained the highest number of shrubs (six per plot). This shadowing effect is well known

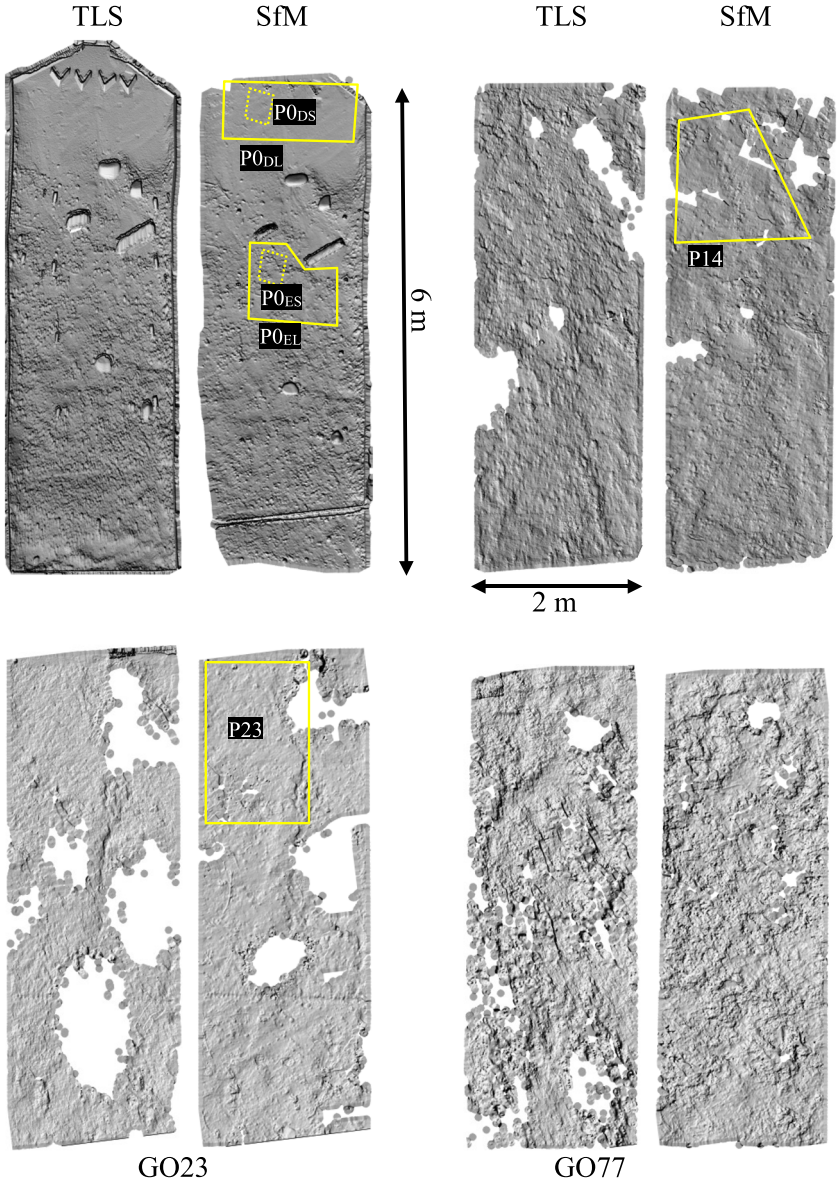

Figure 5. Examples of bare earth surfaces (vegetation filtered out) reconstructed from terrestrial laser scanning (TLS) and Structure-from-Motion (SfM) for 0%, 14%, 23% and 77% ground occlusion (GO). The white holes indicate regions of missing points or sparse point density. The solid and dashed yellow polygons show the outlines of the patches used for the detail cloud comparison. Grid spacing = 1 mm. This figure is available in colour online at wileyonlinelibrary.com/journal/espl

Table III. Missing point gap in three-dimensional (3D) point clouds and elevation differences of TLS–SfM

	TLS %	SfM %	Elevation difference (mm)
GO0	0.70	0	–0.03 ± 5.00
GO14	17.0	0.04	–0.47 ± 4.60
GO23	30.7	0.60	–1.08 ± 13.08
GO53	21.9	0.50	0.01 ± 8.34
GO64	37.8	1.1	–28.3 ± 21.70
GO77	23.0	0	–9.90 ± 21.50

in ground based TLS reconstruction and is typically reduced by scanning the scene of interest from different points of view.

SfM was inherently less susceptible to soil surface occlusion by vegetation because the camera was mobile around the plot. Missing points in the SfM point clouds were primarily caused by inconsistent image matching of vegetation features (Figure 5). In fact, image matching algorithms rely on uniqueness, salience and visibility of interest points in the scene. In pixel regions where vegetation was imaged, pixels were often very similar, resulting in many mismatches and inconsistent 3D positions. These inconsistent 3D blunders were automatically filtered out of the final point cloud by PhotoScan, resulting in incomplete or absent vegetation patches. In the TLS data, stems, branches as well as under-canopy soil surface were reconstructed as long as they were in the line of sight of the laser. With SfM, under-canopy vegetation material and soil surfaces were only reconstructed when the camera was handheld and the oblique configuration allowed these areas to be visible in overlapping images. When the camera was mounted on a pole (near-nadir), plant canopy was reconstructed but was underlain by a gap equivalent to the canopy footprint. This improved soil surface coverage by the converging image configuration explains for example (Table III) the lower occlusion observed on GO53 (0.5%) compared to GO23 (0.6%).

Reconstructions of the GO0 plot presented the opportunity to evaluate the performance of both technologies with no interference from vegetation or larger rock outcroppings. Figure 6 shows the overall comparison between TLS and SfM point clouds. In Figure 6a, the zero-centered distribution of elevation

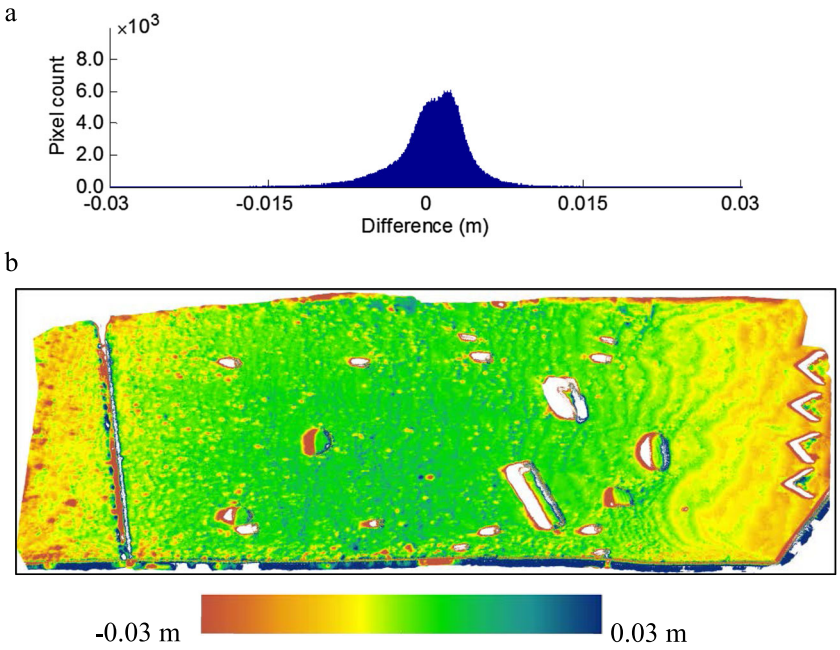

Figure 6. Comparison between TLS and SfM reconstructions for GO0 showing histogram (a) and map (b) of elevation differences between interpolated DEMs at 1 mm grid spacing. This figure is available in colour online at wileyonlinelibrary.com/journal/espl

differences suggests that both technologies generated very similar surfaces. Mean and standard deviation of elevation difference were -3.3×10^{-2} mm and 5 mm (Table III). The DoD map in Figure 6b confirms this match between both surfaces, as areas with more than 10 mm difference between TLS and SfM point clouds mostly occurred in regions that were occluded from the TLS scan position.

Figure 7 shows the histograms of the DoD TLS–SfM on the field data when vegetation was filtered out of the point clouds. The mean and standard deviation of the DoD analyses are summarized in Table III. These results show that increasing vegetation cover tends to decrease agreement between TLS–SfM point clouds. In addition to inherent sources of error associated with TLS and SfM systems, potential factors contributing to this disagreement of TLS–SfM in the field data include: noisy 3D reconstruction in the SfM data due to vegetation, uncertainty associated with the vegetation filtering algorithm and wind action on vegetation resulting in the inclusion of moving features in the SfM reconstruction.

In Figures 6b and 7, a pronounced systematic alternating error pattern (positive–negative–positive or negative–positive–negative) in the downslope direction can be observed on the DoD of plots GO0 and GO23. This error pattern is consistent with projective compensation in image-based reconstruction with low geometric convergence (Mikhail *et al.*, 2001) whereby small errors in camera position are compensated in the numerical optimization process by adjustment of 3D point coordinates. In SfM reconstructions with weakly convergent geometry, this phenomenon often results in a 'doming effect' (Rosnell and Honkavaara, 2012; James and Robson, 2014a; Nouwakpo *et al.*, 2014). In our study, plots GO0, GO23 and GO77 were reconstructed from images taken from the camera mounted on a pole which resulted in a weakly convergent image network and broad scale deformation. On plot GO77, the deformation pattern was present but appeared dampened by the large magnitude of SfM–TLS differences introduced by vegetation on this plot. The ground-based camera (handheld) offered a more convergent image network for GO14, GO53 and GO64 which controlled the deformation problem in these SfM reconstructions.

Spatial statistical analysis

Figures 8 and 9 show the results from the detailed spatial analysis of field and laboratory soil patches. Overall, the semivariograms show that both methods capture similar patterns of spatial variability in surface height, however, semivariances derived from TLS data were systematically higher than those from SfM, an indication that the latter technology produced a smoother surface. The difference maps to the right of the semivariograms show that the reduced semivariance is due to the dynamic range of the SfM surface being suppressed, with peaks and troughs being smoothed out. Patches $P0_{DL}$ and $P0_{EL}$ were considerably smoother than P14 and P23 and the *Y*-axis is an order of magnitude smaller. This was expected because the laboratory soil surface was manually prepared by evenly spreading the soil over the plot, leading to an inherently smoother surface than that observed in natural field conditions.

Semivariogram parameters calculated for each laboratory patch (P0) (Table IV) show the presence of a nugget with TLS but not with SfM. Many authors have reported the absence of nugget effect in soil surface data when a small grid sample is used (e.g. Linden and Vandoren, 1986; Helming *et al.*, 1993; Vermang *et al.*, 2013). While the absence of nugget in the SfM might appear to be beneficial, it is more likely an indication that the SfM surface is smoothly interpolated at the finest scales rather than representing unique height estimates. For the field patches (P14 and P23), no nugget effect was present in the TLS data, likely a result of the vegetation filtering algorithm (Figure 8 and Table IV). The SfM-derived semivariogram for P14 revealed a nugget effect resulting from fitting a Gaussian semivariogram model to this data. At very small lag distances, the Gaussian model overestimated observed variance, leading to an artifactual nugget effect.

The larger nugget effect in the TLS data observed on the large patches ($P0_{DL}$ and $P0_{EL}$) compared to the small patches ($P0_{DS}$ and $P0_{ES}$) is the result of the downsampling of the large patches to 20 000 points which did not capture variability at very small lag distances. The TLS-derived variogram for the full-resolution smooth surface $P0_{DS}$ in Figure 10a shows the actual limit of TLS precision, where the nugget variance corresponds

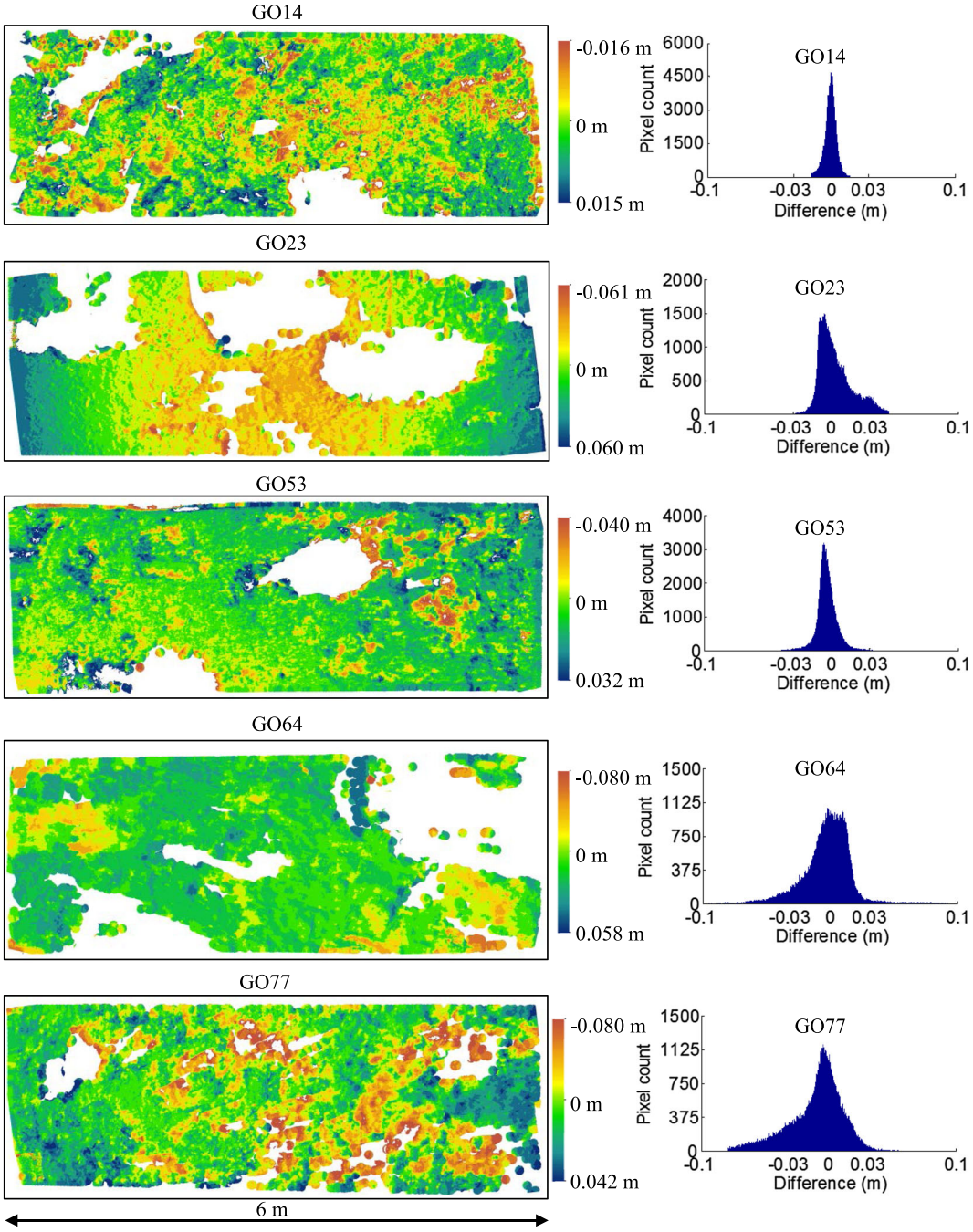

Figure 7. Results of the TLS–SfM comparison showing maps of difference of digital elevation model (DoD) at 1 mm grid spacing for the field plots (GO14, GO23, GO53, GO64, GO77) and the corresponding histograms of elevation difference. This figure is available in colour online at wileyonlinelibrary.com/journal/espl

to a standard deviation between adjacent points of 1 mm, a value well within the 2 mm nominal precision of the Scanstation 2 instrument. This indicates that some of the nugget variance in Figure 9a was a combined effect of surface variability and the downsampling. For the pebbly surface in Figure 10b, the higher nugget variance observed by the TLS system is expected with the abrupt edges and overhangs of pebbles increasing the standard deviation between adjacent points to 2.3 mm in height.

The decrease in roughness from the active erosion area ($P0_{ES}$ and $P0_{EL}$) to the deposition area ($P0_{DS}$ and $P0_{DL}$), was detected in both TLS and SfM data (Figures 9 and 10) and indicated by a lower sill of the semivariogram in the deposition area. Semivariogram ranges (area of influence of a spatial point) were similar between technologies for the same patches in laboratory conditions (Table IV). At both sampling densities ranges obtained for the deposition zone were larger than those obtained for the actively eroding area. In the deposition area, these ranges represent the average period of long wave undulations that often characterize deposition deltas as shallow secondary channels form in deposited material. This repeating pattern explains the decrease in semivariance of $P0_{DL}$ beyond for lag distances larger than the range (Figure 9a). At the dense sampling rate, observed semivariogram ranges in the active erosion patch ($P0_{ES}$) can be related to individual rock sizes (23 mm on average).

Discussion

Sources of error

Differences in sources of error and uncertainty propagation models between TLS and SfM technologies explain disparities

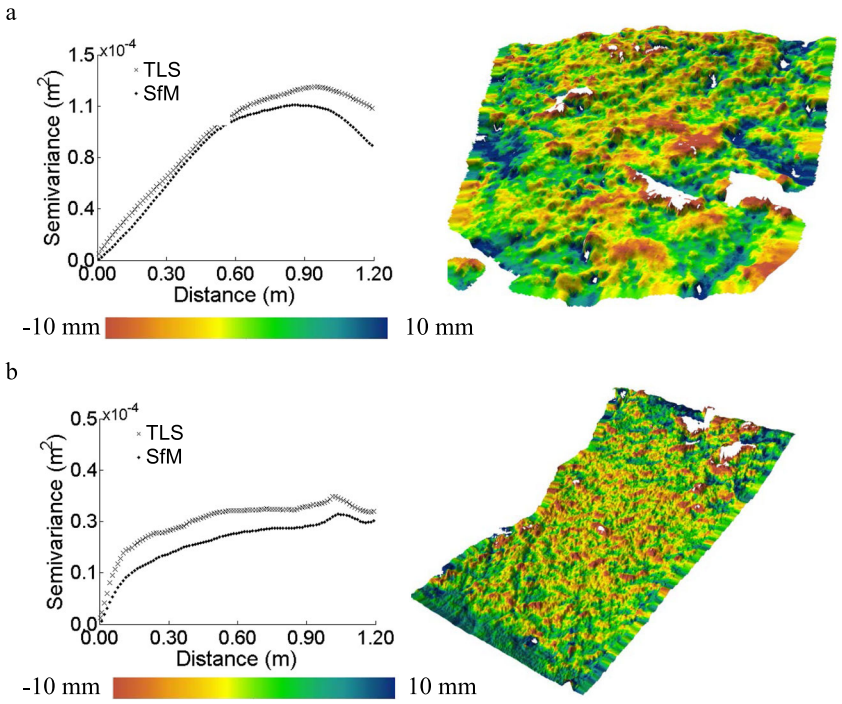

Figure 8. Semivariogram of elevation values and map of elevation differences (1 mm grid spacing) between SfM and TLS points (ZSfM–ZTLS) for patches P14 (a) and P23 (b). The difference maps are shaded with TLS-derived microtopography at a vertical exaggeration ratio of two. This figure is available in colour online at wileyonlinelibrary.com/journal/espl

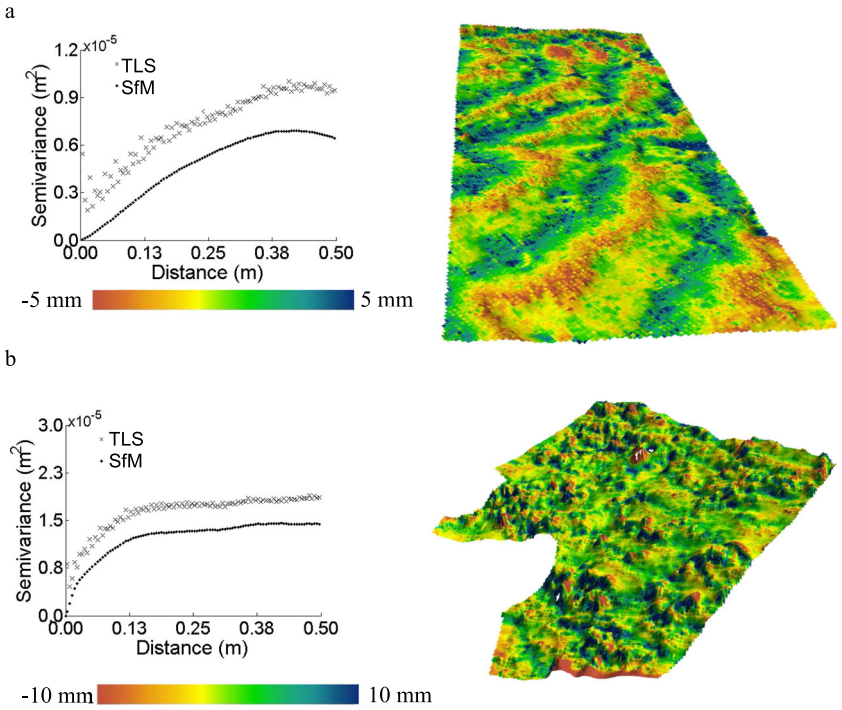

Figure 9. Semivariogram of elevation values and map of elevation differences (1 mm grid spacing) between SfM and TLS points (ZSfM–ZTLS) for patches $P0_{DL}$ (a) and $P0_{EL}$ (b). The difference maps are shaded with TLS-derived microtopography at a vertical exaggeration ratio of two. This figure is available in colour online at wileyonlinelibrary.com/journal/espl

in reconstructed surface smoothness. In SfM, the critical step of point matching relies on the relative color distribution throughout each image. Since neighboring points likely lie on similar regions of the color spectrum, computed 3D point positions in SfM are inherently influenced by loss of details due to analog to digital conversion and the RGB (red, green, and blue) value interpolations that occur at the image sensor level. These processes tend to smooth out irregularities from SfM-derived surfaces. This smoothing does not occur with the TLS since each point is determined from an independent range (distance) and angle measurement, leading to a surface that preserves fine-scale details.

Plot scale comparisons between TLS and image-based systems for 3D soil surface reconstructions have been carried out by only a few authors (e.g. Heng *et al.*, 2010; Castillo *et al.*, 2012). These studies including the one presented in this article assume TLS to be a benchmark technology for evaluation of image-based technologies. In our study, the standard deviation

Table IV. Best fitting parameters of surface patch semivariograms assuming an exponential model

		Sill (m^2)	Nugget (m^2)	Partial sill (m^2)	Range (m)	Effective range (m)
$P0_{DS}$	TLS	2.32×10^{-6}	9.00×10^{-7}	1.42×10^{-6}	5.80×10^{-2}	1.74×10^{-1}
	SfM	1.13×10^{-6}	0	1.13×10^{-6}	5.80×10^{-2}	1.74×10^{-1}
$P0_{ES}$	TLS	1.03×10^{-5}	5.22×10^{-6}	5.06×10^{-6}	2.31×10^{-2}	6.94×10^{-2}
	SfM	6.56×10^{-6}	0	6.56×10^{-6}	2.23×10^{-2}	6.69×10^{-2}
$P0_{DL}$	TLS	1.23×10^{-5}	2.43×10^{-6}	9.84×10^{-6}	1.87×10^{-1}	5.62×10^{-1}
	SfM	8.42×10^{-6}	0	8.42×10^{-6}	1.80×10^{-1}	5.40×10^{-1}
$P0_{EL}$	TLS	3.18×10^{-5}	6.35×10^{-6}	2.54×10^{-5}	1.50×10^{-1}	4.50×10^{-1}
	SfM	2.66×10^{-5}	0	2.66×10^{-5}	1.42×10^{-1}	4.27×10^{-1}
P14[a]	TLS	1.38×10^{-4}	0	1.38×10^{-4}	4.40×10^{-1}	9.80×10^{-1}
	SfM	1.07×10^{-4}	5.49×10^{-6}	1.01×10^{-4}	3.60×10^{-1}	6.24×10^{-1}
P23	TLS	2.81×10^{-5}	0	2.81×10^{-5}	1.40×10^{-1}	4.19×10^{-1}
	SfM	2.49×10^{-5}	0	2.49×10^{-5}	2.54×10^{-1}	7.61×10^{-1}

[a]Gaussian semivariogram model used for best fit.

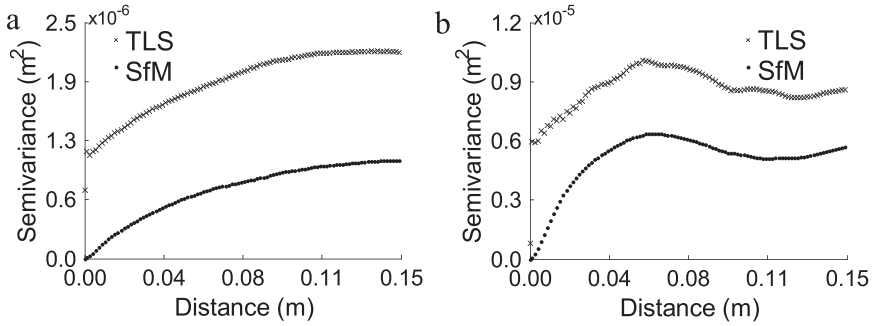

Figure 10. Semivariogram of elevation values of TLS and SfM points for patches $P0_{DS}$ (a) and $P0_{ES}$ (b).

of elevation difference between TLS and SfM DEM of 5 mm on the least vegetated plots (GO0 and GO14) was higher but in the same order of magnitude as that obtained by Heng *et al.* (2010) (3.5 mm) in similar conditions (bare laboratory plot). Even when the systematic doming effect was removed from the GO0 plot error map with a two-dimensional second-order polynomial (Figure 11), the RMSE of the SfM–TLS differences was marginally impacted and remained at 5 mm. These results suggest that agreement between surfaces derived from image-based systems and TLS might be limited by sources of error inherent to each technology. It is important to note that Heng *et al.* (2010) used a traditional photogrammetric approach

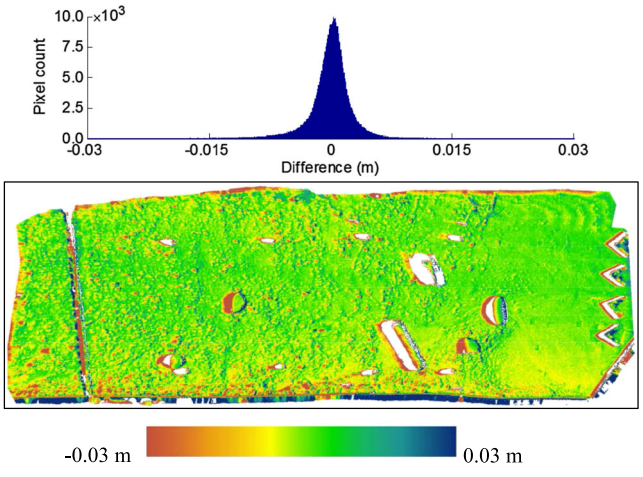

Figure 11. Comparison between TLS and SfM reconstructions for GO0 after removal of systematic 'doming' effect with a two-dimensional polynomial fit. (a) Histogram of the comparison. (b) Map of difference of digital elevation model (DoD) at 1 mm grid spacing. This figure is available in colour online at wileyonlinelibrary.com/journal/espl

which typically results in better accuracy than the SfM used in this article but at the cost of increased complexity.

In the TLS system, the most dominant source of error likely arises from the range measurement function. A close examination of the surface reconstructed for the GO0 plot (Figure 12) showed that when ground features (e.g. broken branch, wooden stake) create a partial occlusion zone, points located at the perimeter of the occlusion boundary are poorly reconstructed, resulting in a trail of erroneous points scattered across the occlusion envelope. A possible explanation of this phenomenon is that at these occlusion boundaries, the laser footprint straddled foreground and background points leading to multiple laser pulse echoes inaccurately processed by the instrument. This type of aberration is likely a major source of error in TLS-derived field surfaces where occlusion by vegetation is significant and could be reduced by adopting a multi-view scanning strategy coupled with an adequate blunder detection scheme.

In addition to these technology-specific error sources are point cloud registration errors. This error type is difficult to rigorously quantify from our data due to the confounding effect of error sources described earlier. In fact ICP registration errors expressed as final point-to-point distance RMS were within the same order of magnitude as the DoD standard deviations for all plots. Nevertheless one can approximate actual point cloud registration errors to the 2.5 mm RMSE of the GCPs in the PhotoScan workflow since ground coordinates of these GCPs were determined with a total station, a non-automated version of TLS.

SfM-derived surfaces suffered plot scale accuracy problems expressed as plot-scale warping which can be very serious depending on the intended use of the reconstruction. Others (e.g. Fonstad *et al.*, 2013; James and Robson, 2014a; Nouwakpo *et al.*, 2014) have also reported similar deformations in SfM-based reconstructions especially when the image

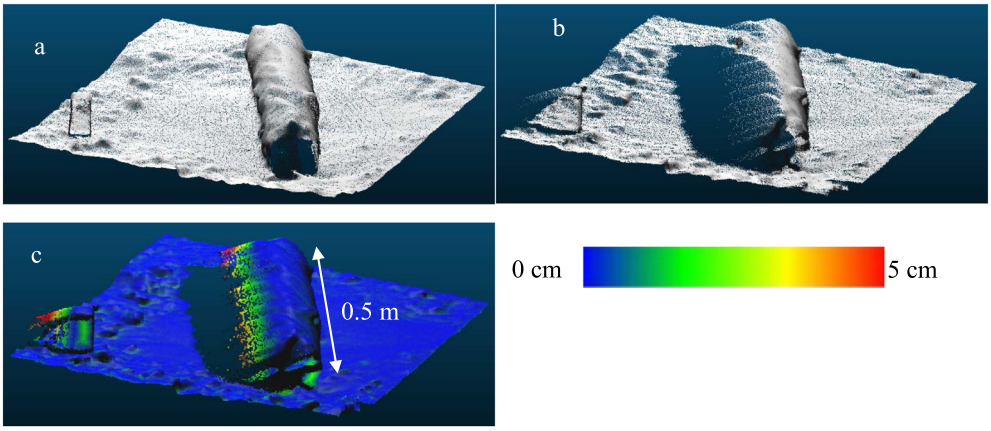

Figure 12. Close-up image of decimeter scale ground features reconstructed by SfM (a), TLS (b) and distance map SfM–TLS surface (c). Note trailing TLS points off sharp edge of the log (center) and stake (far left). This figure is available in colour online at wileyonlinelibrary.com/journal/espl

network produced near-parallel imaging directions. The problem of projective compensation leading to these deformations is typically reduced in traditional photogrammetry with a judicious selection of GCPs used to constrain the least square adjustment. This dependence of traditional photogrammetry on GCPs was alleviated by SfM but at the cost of accuracy. Nevertheless, to be useful for most applications, SfM-derived soil surfaces have to be geo-referenced into metric coordinate systems by means of GCPs. A careful distribution of GCPs across the soil surface can serve as a quality check of the overall accuracy by evaluating spatial trends in GCP residuals. In addition, by distributing GCPs across a range of elevation one can better capture the dynamic range of the soil surface with SfM. Alternatively, James and Robson (2014a) demonstrated that the inclusion of oblique images in a network of predominantly near-parallel imaging directions reduced DEM errors.

Application considerations

In this study, point clouds containing variable levels of vegetation were obtained using SfM and TLS. An increase in shrub cover resulted in significant GO in the TLS data but the 3D distribution of shrubs was captured. In the SfM data, shrubs were only reconstructed when image texture in shrub regions allowed successful feature matching. The effect of shrub on soil surface reconstruction seems therefore to be limited to occlusion. Spatial coverage of TLS data is controlled by obstructions relative to the TLS view point and will therefore depend on canopy height, diameter and spatial distribution. In the SfM data, the main shrub characteristic controlling spatial coverage of soil surface is canopy diameter and spatial distribution. One can imagine, nevertheless, the existence of a maximum shrub height beyond which plot scale SfM becomes impractical and requires more complex camera support systems such as unmanned aerial vehicles. From field experience, we estimate this maximum shrub height to be around 1 m.

In contrast to shrubs, grasses and isolated litter debris can generate noise in the soil surface data. In the TLS data, individual grass strands and litter debris were often reconstructed in areas where they were absent in the SfM data due to the sensor level attenuation occurring in digital cameras. This high frequency noise can be easily removed from TLS data using low pass filters. As grass cover increases, soil surface signal-to-noise ratio significantly decreases in both TLS and SfM. A similar increase in the noise of photogrammetric surface elevation models was reported by Rossi and Ares (2012a). At high grass cover, the soil surface is completely invisible and SfM or TLS reconstructions were of little value for soil erosion application. For example, in our study, the GO77 plot was reconstructed as a dense point cloud of grass pixels with no clearly defined soil surface feature. Nevertheless, since grass cover increase is inversely related to soil erosion processes, soil microtopography information on high grass cover plots is of limited interest for understanding sediment transport processes.

With an average camera – ground distance of 2.34 m, the 0.24 mm vertical precision achieved in this study is equivalent to a 1:11 700 relative precision ratio, better than the 1:6400 scale precision ratio obtained by James and Robson (2012) on a centimeter scale geologic rock sample. The better relative precision ratio obtained in our study is the result of two possible factors. First, the more complete distortion model used in PhotoScan compared to the single radial distortion parameter implemented in the freely available SfM software used in James and Robson (2012) may have performed better at reconstructing scene geometry. A second factor explaining our improved relative precision ratio compared to that of James and Robson (2012) is the use in our study of repeat estimates of GCPs to calculate precision thereby reducing potential errors introduced by the independent total station measurements. In James and Robson (2012), precision estimates may have been confounded by other factors such as precision of the independent laser scanner measurement used as benchmark and potential errors in the ICP method used to register their SfM reconstruction with laser scanner outputs.

Elevation change precisions are important for adequate interpretation of detected geomorphic changes. For sediment budget estimation, they can be used to define simple threshold values for erosion – deposition measurement assuming a spatially uniform error distribution (e.g. Nouwakpo and Huang, 2012b) or used in more complex error propagation schemes such as the fuzzy interference system proposed by Wheaton *et al.* (2010). Assuming a simple error propagation rule (i.e. no interaction between error sources), the 0.2 mm vertical precision of the SfM data estimated from the repeat reconstructions would result in a 0.28 mm precision for change detection. For the TLS data however, vertical measurement precision is not directly available from the instrument output. In theory, it is possible to determine achieved precision in the TLS point cloud by applying error propagation functions to distances and angles measured by the instrument for each individual point but angle measurements were not included in the TLS output. In addition, the 1 mm average point spacing adopted was insufficient to allow precise identification of stable points

from the repeat TLS measures which would have been to estimate precision. Nevertheless, a nominal surface model precision of 2 mm was provided by the manufacturer for the TLS instrument. A 2 mm measurement precision suggests a change detection threshold of 2.8 mm for the TLS data. This value is one order of magnitude larger than that achieved with the SfM method and would limit the usefulness of TLS in tracking millimeter-scale changes to soil microtopography that occur during erosive events.

Practical considerations

During our field tests, each TLS scan took approximately 15 minutes for the 6 m × 2 m plot. To reduce the effect of occlusion on final reconstruction, it was estimated that each plot would have required a minimum of four scan positions given the type and density of vegetative cover. Assuming that this four-corner scanning scheme was feasible, a minimum of one hour of scan time would have been required per plot. In addition to this scan time, is the time needed to move and setup the instrument at each scan position. A rough estimate of the total time required to acquire one plot reconstruction using the four-corner scanning scheme is two hours. In contrast, taking pictures for the SfM reconstruction only took 15 minutes per plot. This lower data acquisition time is a crucial advantage of SfM for experimental field research.

While the TLS output was a point cloud that is immediately available for analysis, the SfM data is simply a series of overlapping pictures that needed to be processed into a 3D point cloud. This processing step required on average four hours of computing time to generate a dense point cloud. In addition to this, GCP image coordinates had to be measured in the images to produce a reliable transformation into metric coordinate. Automating the GCP detection process in the images proved challenging due to the highly textured soil surface (many rock fragments and vegetation) dominating image feature. A minimum of two hours of operator time was required for a manual detection and labelling of these image GCPs per plot. Assuming a low monetary cost of computation time, the 1.75 hours saved in the field per plot was regained as time needed for the manual GCP detection. However considering that the cost of time spent in the field is often several orders of magnitude larger than that spent in the laboratory, SfM is likely still cost-competitive for field research compared to TLS. It is important to note that a four-corner TLS scanning scheme would require some post processing and quality check measures to merge all partial point clouds into one complete cloud. Furthermore, soil microtopography changes are assessed at the millimeter-scale and are extremely sensitive to systematic errors which may be introduced during the TLS instrument's travel through survey positions.

In this study, we found that SfM reconstructions are susceptible to plot scale deformations that could severely undermine accuracy of measured surface processes. This type of deformation can be detected and corrected with GCPs independently measured with high accuracy. Since some of these GCPs need to be in the interior of the erosion plot, they interfere with flow paths and sediment transport processes. This drawback of SfM compared to TLS can be reduced by installing GCPs away from flow concentration pathways. It may also be possible to combine the ability of TLS to capture the full dynamic range of the surface in an unbiased way with the ability of handheld photography to rapidly cover the plot and avoid occlusion by plants. A single view of the plot with TLS or a sparse set of points surveyed with a total station would likely have enough information to correct the long distance deformation of the SfM model seen in Figures 6b and 7. It may also be possible to very realistically boost the dynamic range of fine scale features in the SfM surface by histogram matching to surface heights observed in local neighborhoods by the TLS. Alternatively, co-kriging could be used to interpolate a surface based on the structure of correlation between co-registered SfM and TLS surfaces. This hybrid approach might be much more practical than acquiring data from multiple TLS viewpoints, particularly if there is an experimental structure like a rainfall simulator in operation that would block access.

Conclusions

This study evaluated the performance of SfM and TLS at reconstructing soil surface with a range of ground covers on naturally vegetated erosion plots. The single viewpoint TLS strategy adopted was more susceptible to GO than SfM which inherently offered better spatial coverage because the camera was mobile around the digitized surface.

Agreement between TLS and SfM surfaces was best on the bare laboratory surface with an average elevation difference between the two technologies of 0.03 ± 5 mm. Nevertheless, some along track distortion was observed in the SfM data which highlights the importance of quality check measures such as judiciously place GCPs in image based reconstruction systems. As vegetation cover increased, agreement between TLS and SfM degraded but was dramatically affected beyond 53% of ground cover.

Detailed semivariogram analysis on meter-square-scale surface patches showed that TLS and SfM surfaces were very similar even on highly vegetated surfaces. However, excessive smoothing of the SfM-derived surfaces resulted in a narrowing of the dynamic range and loss of fine scale details with this technology.

Errors in the TLS data were mainly caused by the distance measurement function of the instrument especially at the fringe of occlusion regions where laser light intersect foreground and background features simultaneously. From this study, we found that by combining the practical advantage of SfM with the inherently high precision of TLS-like technologies such as total station, one could achieve soil surface reconstructions of adequate quality for geoscience and ecohydrology applications.

References

Agisoft LLC. 2013. *Agisoft photoscan professional edition*. Agisoft LLC: St Petersburg.

Aguilar MA, Aguilar FJ, Negreiros J. 2009. Off-the-shelf laser scanning and close-range digital photogrammetry for measuring agricultural soils microrelief. *Biosystems Engineering* **103**: 504–517. DOI: 10.1016/j.biosystemseng.2009.02.010

Barker R, Dixon L, Hooke J. 1997. Use of terrestrial photogrammetry for monitoring and measuring bank erosion. *Earth Surface Processes and Landforms* **22**: 1217–1227. DOI: 10.1002/(sici)1096-9837(199724)22:13<1217::aid-esp819>3.0.co;2-u

Bay H, Tuytelaars T, Van Gool L. 2006. *Surf: Speeded up Robust Features*. Computer vision–eccv 2006. Springer: Berlin; 404–417.

Berger C, Schulze M, Rieke-Zapp D, Schlunegger F. 2010. Rill development and soil erosion: a laboratory study of slope and rainfall intensity. *Earth Surface Processes and Landforms* **35**: 1456–1467. DOI: 10.1002/esp.1989

Brasington J, Smart RMA. 2003. Close range digital photogrammetric analysis of experimental drainage basin evolution. *Earth Surface Processes and Landforms* **28**: 231–247. DOI: 10.1002/esp.480

Brasington J, Vericat D, Rychkov I. 2012. Modeling river bed morphology, roughness, and surface sedimentology using high resolution terrestrial laser scanning. *Water Resources Research* **48**: 18. DOI: 10.1029/2012wr012223

Brodu N, Lague D. 2012. 3D terrestrial lidar data classification of complex natural scenes using a multi-scale dimensionality criterion: applications in geomorphology. *Isprs Journal of Photogrammetry and Remote Sensing* **68**: 121–134. DOI: 10.1016/j.isprsjprs.2012.01.006

Castillo C, Perez R, James MR, Quinton JN, Taguas EV, Gomez JA. 2012. Comparing the accuracy of several field methods for measuring gully erosion. *Soil Science Society of America Journal* **76**: 1319–1332. DOI: 10.2136/sssaj2011.0390

Collins SH, Moon GC. 1979. Stereometric measurement of streambank erosion. *Photogrammetric Engineering and Remote Sensing* **45**: 183–190.

Cressie N, Wikle CK. 2011. *Statistics for Spatio-temporal Data*. John Wiley & Sons: Chichester.

Darboux FH, Huang C. 2003. An instantaneous-profile laser scanner to measure soil surface microtopography. *Soil Science Society of America Journal* **67**: 92–99.

Eitel JUH, Williams CJ, Vierling LA, Al-Hamdan OZ, Pierson FB. 2011. Suitability of terrestrial laser scanning for studying surface roughness effects on concentrated flow erosion processes in rangelands. *Catena* **87**: 398–407. DOI: 10.1016/j.catena.2011.07.009

Elliot WJ, Laflen JM, Thomas AW, Kohl KD. 1997. Photogrammetric and rillmeter techniques for hydraulic measurement in soil erosion studies. *Transactions of the ASAE* **40**: 157–165.

Fonstad MA, Dietrich JT, Courville BC, Jensen JL, Carbonneau PE. 2013. Topographic structure from motion: a new development in photogrammetric measurement. *Earth Surface Processes and Landforms* **38**: 421–430. DOI: 10.1002/esp.3366

General Public Licence. 2014. Cloudcompare v2.5. General Public Licence.

Gomez-Gutierrez A, Schnabel S, Berenguer-Sempere F, Lavado-Contador F, Rubio-Delgado J. 2014. Using 3d photo-reconstruction methods to estimate gully headcut erosion. *Catena* **120**: 91–101. DOI: 10.1016/j.catena.2014.04.004

Guzha AC. 2004. Effects of tillage on soil microrelief, surface depression storage and soil water storage. *Soil and Tillage Research* **76**: 105–114. DOI: 10.1016/j.still.2003.09.002

Harris C, Stephens M. 1988. A combined corner and edge detector. *Proceedings, Alvey Vision Conference*, Manchester, UK.

Helming K, Romkens MJM, Prasad SN. 1998. Surface roughness related processes of runoff and soil loss: a flume study. *Soil Science Society of America Journal* **62**: 243–250.

Helming K, Roth CH, Wolf R, Diestel H. 1993. Characterization of rainfall – microrelief interactions with runoff using parameters derived from digital elevation models (dems). *Soil Technology* **6**: 273–286. DOI: 10.1016/0933-3630(93)90016-8

Heng BCP, Chandler JH, Armstrong A. 2010. Applying close range digital photogrammetry in soil erosion studies. *Photogrammetric Record* **25**: 240–265.

Heng BCP, Sander GC, Armstrong A, Quinton JN, Chandler JH, Scott CF. 2011. Modeling the dynamics of soil erosion and size-selective sediment transport over nonuniform topography in flume-scale experiments. *Water Resources Research* **47**. Article no. W02513. DOI: 10.1029/2010wr009375

James MR, Quinton JN. 2014. Ultra-rapid topographic surveying for complex environments: the hand-held mobile laser scanner (HMLS). *Earth Surface Processes and Landforms* **39**: 138–142. DOI: 10.1002/esp.3489

James MR, Robson S. 2012. Straightforward reconstruction of 3d surfaces and topography with a camera: accuracy and geoscience application. *Journal of Geophysical Research, Earth Surface* **117**. Article no. F03017. DOI: 10.1029/2011JF002289

James MR, Robson S. 2014a. Mitigating systematic error in topographic models derived from uav and ground-based image networks. *Earth Surface Processes and Landforms* **39**: 1413–1420. DOI: 10.1002/esp.3609

James MR, Robson S. 2014b. Sequential digital elevation models of active lava flows from ground-based stereo time-lapse imagery. *Isprs Journal of Photogrammetry and Remote Sensing* **97**: 160–170. DOI: 10.1016/j.isprsjprs.2014.08.011

Javemick L, Brasington J, Caruso B. 2014. Modeling the topography of shallow braided rivers using structure-from-motion photogrammetry. *Geomorphology* **213**: 166–182. DOI: 10.1016/j.geomorph.2014.01.006

Jester W, Klik A. 2005. Soil surface roughness measurement – methods, applicability, and surface representation. *Catena* **64**: 174–192. DOI: 10.1016/j.catena.2005.08.005

Johnson K, Nissen E, Saripalli S, Arrowsmith JR, McGarey P, Scharer K, Williams P, Blisniuk K. 2014. Rapid mapping of ultrafine fault zone topography with structure from motion. *Geosphere* **10**: 969–986. DOI: 10.1130/ges01017.1

Kaiser A, Neugirg F, Rock G, Muller C, Haas F, Ries J, Schmidt J. 2014. Small-scale surface reconstruction and volume calculation of soil erosion in complex Moroccan gully morphology using structure from motion. *Remote Sensing* **6**: 7050–7080. DOI: 10.3390/rs6087050

Kincaid DR, Williams G. 1966. Rainfall effects on soil surface characteristics following range improvement treatments. *Journal of Range Management* **19**: 346–351. DOI: 10.2307/3895569

Lague D, Brodu N, Leroux J. 2013. Accurate 3d comparison of complex topography with terrestrial laser scanner: application to the rangitikei canyon (n-z). *Isprs Journal of Photogrammetry and Remote Sensing* **82**: 10–26. DOI: 10.1016/j.isprsjprs.2013.04.009

Leica Geosystems. 2006. *Leica Photogrammetry Suite Project Manager*. Leica Geosystems Geospatial Imaging: Norcross, GA.

Linden DR, Vandoren DM. 1986. Parameters for characterizing tillage-induced soil surface roughness. *Soil Science Society of America Journal* **50**: 1560–1565.

Lo CP, Wong FY. 1973. Microscale geomorphology features. *Photogrammetric Engineering and Remote Sensing* **39**: 1289–1296.

Lowe DG. 1999. Object recognition from local scale-invariant features. *Proceedings of the Seventh IEEE International Conference, Computer Vision, 1999*, September 20–27, Kerkyra; 1150–1157.

Mancini F, Dubbini M, Gattelli M, Stecchi F, Fabbri S, Gabbianelli G. 2013. Using unmanned aerial vehicles (UAV) for high-resolution reconstruction of topography: the structure from motion approach on coastal environments. *Remote Sensing* **5**: 6880–6898. DOI: 10.3390/rs5126880

Marzolff I, Poesen J. 2009. The potential of 3d gully monitoring with gis using high-resolution aerial photography and a digital photogrammetry system. *Geomorphology* **111**: 48–60. DOI: 10.1016/j.geomorph.2008.05.047

Mikhail EM, Bethel JS, McGlone JC. 2001. *Introduction to Modern Photogrammetry*. Wiley: New York.

Moreno RG, Álvarez MCD, Alonso AT, Barrington S, Requejo AS. 2008. Tillage and soil type effects on soil surface roughness at semiarid climatic conditions. *Soil and Tillage Research* **98**: 35–44. DOI: 10.1016/j.still.2007.10.006

Nouwakpo SK, Huang C. 2012a. A simplified close-range photogrammetric technique for soil erosion assessment. *Soil Science Society of America Journal* **76**: 70–84.

Nouwakpo SK, Huang CH. 2012b. The role of subsurface hydrology in soil erosion and channel network development on a laboratory hillslope. *Soil Science Society of America Journal* **76**: 1197–1211. DOI: 10.2136/sssaj2012.0013

Nouwakpo SK, James MR, Weltz MA, Huang C-H, Chagas I, Lima L. 2014. Evaluation of structure from motion for soil microtopography measurement. *The Photogrammetric Record* **29**: 297–316. DOI: 10.1111/phor.12072

Ouedraogo MM, Degre A, Debouche C, Lisein J. 2014. The evaluation of unmanned aerial system-based photogrammetry and terrestrial laser scanning to generate dems of agricultural watersheds. *Geomorphology* **214**: 339–355. DOI: 10.1016/j.geomorph.2014.02.016

Paige GB, Stone JJ, Smith JR, Kennedy JR. 2004. The walnut gulch rainfall simulator: a computer-controlled variable intensity rainfall simulator. *Applied Engineering in Agriculture* **20**: 25–31.

Rieke-Zapp DH, Nearing MA. 2005. Digital close range photogrammetry for measurement of soil erosion. *The Photogrammetric Record* **20**: 69–87.

Ries JB, Marzolff I. 2003. Monitoring of gully erosion in the central ebro basin by large-scale aerial photography taken from a remotely controlled blimp. *Catena* **50**: 309–328. Article no. L19402. DOI: 10.1016/s0341-8162(02)00133-9

Roering JJ, Stimely LL, Mackey BH, Schmidt DA. 2009. Using dinsar, airborne lidar, and archival air photos to quantify landsliding and

sediment transport. *Geophysical Research Letters* **36**. Article no. L19402. DOI: 10.1029/2009gl040374

Romkens MJM, Helming K, Prasad SN. 2001. Soil erosion under different rainfall intensities, surface roughness, and soil water regimes. *Catena* **46**: 103–123. DOI: 10.1016/s0341-8162(01)00161-8

Rosnell T, Honkavaara E. 2012. Point cloud generation from aerial image data acquired by a quadrocopter type micro unmanned aerial vehicle and a digital still camera. *Sensors* **12**: 453–480. DOI: 10.3390/s120100453

Rossi MJ, Ares JO. 2012a. Close range stereophotogrammetry and video imagery analyses in soil ecohydrology modelling. *Photogrammetric Record* **26**: 111–126. DOI: 10.1111/j.1477-9730.2012.00672.x

Rossi MJ, Ares JO. 2012b. Depression storage and infiltration effects on overland flow depth-velocity-friction at desert conditions: field plot results and model. *Hydrology and Earth System Sciences* **16**: 3293–3307. DOI: 10.5194/hess-16-3293-2012

Rychkov I, Brasington J, Vericat D. 2012. Computational and methodological aspects of terrestrial surface analysis based on point clouds. *Computers & Geosciences* **42**: 64–70. DOI: 10.1016/j.cageo.2012.02.011

Sankey JB, Ravi S, Wallace CSA, Webb RH, Huxman TE. 2012. Quantifying soil surface change in degraded drylands: shrub encroachment and effects of fire and vegetation removal in a desert grassland. *Journal of Geophysical Research-Biogeosciences* **117**: 1–11. DOI: 10.1029/2012jg002002

Schneider A, Gerke HH, Maurer T, Nenov R. 2013. Initial hydrogeomorphic development and rill network evolution in an artificial catchment. *Earth Surface Processes and Landforms* **38**: 1496–1512. DOI: 10.1002/esp.3384

Schuenemeyer J, Drew L. 2011. *Statistics for Earth and Environmental Scientists*. John Wiley & Sons: Chichester.

Thompson SE, Katul GG, Porporato A. 2010. Role of microtopography in rainfall-runoff partitioning: an analysis using idealized geometry. *Water Resources Research* **46**. Article no. W07520. DOI: 10.1029/2009wr008835

Toy TJ, Foster GR, Renard KG. 2002. *Soil Erosion: Processes, Prediction, Measurement, and Control*. John Wiley & Sons: Chichester.

Valentine WH, Cook M. 1979. Monitoring cut slope erosion by close-range photogrammetry. *Photogrammetric Engineering and Remote Sensing* **45**: 788–788.

Vermang J, Norton LD, Baetens JM, Huang C, Cornelis WM, Gabriels D. 2013. Quantification of soil surface roughness evolution under simulated rainfall. *Transactions of the ASABE* **56**: 505–514.

Westoby MJ, Brasington J, Glasser NF, Hambrey MJ, Reynolds JM. 2012. 'Structure-from-motion' photogrammetry: a low-cost, effective tool for geoscience applications. *Geomorphology* **179**: 300–314. DOI: 10.1016/j.geomorph.2012.08.021

Wheaton JM, Brasington J, Darby SE, Sear DA. 2010. Accounting for uncertainty in dems from repeat topographic surveys: improved sediment budgets. *Earth Surface Processes and Landforms* **35**: 136–156. DOI: 10.1002/esp.1886